



## Article

# Severe Biomass-Burning Aerosol Pollution during the 2019 Amazon Wildfire and Its Direct Radiative-Forcing Impact: A Space Perspective from MODIS Retrievals

Shuyun Yuan <sup>1,2</sup>, Fangwen Bao <sup>2</sup>, Xiaochuan Zhang <sup>2</sup> and Ying Li <sup>2,3,\*</sup>

<sup>1</sup> School of Environment, Harbin Institute of Technology, Harbin 150059, China; 11749326@mail.sustech.edu.cn

<sup>2</sup> Center for Oceanic and Atmospheric Science at SUSTech (COAST), Department of Ocean Sciences and Engineering, Southern University of Science and Technology, Shenzhen 518055, China; baofw@sustech.edu.cn (F.B.); zhangxc3@mail.sustech.edu.cn (X.Z.)

<sup>3</sup> Southern Marine Science and Engineering Guangdong Laboratory (Guangzhou), Guangzhou 511458, China

\* Correspondence: liy66@sustech.edu.cn

**Abstract:** An extreme biomass burning event occurred in the Amazonian rainforest from July through September 2019 due to the extensive wildfires used to clear the land, which allowed for more significant forest burning than previously occurred. In this study, we reclustered the clear-sky ambient aerosols to adapt the black carbon (BC) aerosol retrieval algorithm to Amazonia. This not only isolated the volumetric fraction of BC ( $f_{bc}$ ) from moderate-resolution imaging spectroradiometer (MODIS) aerosol data, but also facilitated the use of aerosol mixing and scattering models to estimate the absorption properties of smoke plumes. The retrieved MODIS aerosol dataset provided a space perspective on characterizing the aerosol changes and trends of the 2019 pollution event. A very high aerosol optical depth (AOD) was found to affect the source areas continuously, with higher and thus stronger aerosol absorption. These pollutants also affected the atmosphere downwind due to the transport of air masses. In addition, properties of aerosols emitted from the 2019 Amazonian wildfire events visualized a significant year-to-year enhancement, with the averaged AOD at 550 nm increased by 150%. A 200% increase in the aerosol-absorption optical depth (AAOD) at 550 nm was recognized due to the low single-scattering albedo (SSA) caused by the explosive BC emissions during the pollution peak. Further simulations of aerosol radiative forcing (ARF) showed that the biomass-burning aerosols emitted during the extreme Amazonian wildfires event in 2019 forced a significant change in the radiative balance, which not only produced greater heating of the atmospheric column through strong absorption of BC, but also reduced the radiation reaching the top-of-atmosphere (TOA) and surface level. The negative radiative forcing at the TOA and surface level, as well as the positive radiative forcing in the atmosphere, were elevated by ~30% across the whole of South America compared to 2018. These radiative effects of the absorbing aerosol could have the ability to accelerate the deterioration cycle of drought and fire over the Amazonian rainforest.

**Keywords:** satellite remote sensing; Amazon wildfire; black carbon; direct radiative forcing; aerosol optical properties



**Citation:** Yuan, S.; Bao, F.; Zhang, X.; Li, Y. Severe Biomass-Burning Aerosol Pollution during the 2019 Amazon Wildfire and Its Direct Radiative-Forcing Impact: A Space Perspective from MODIS Retrievals. *Remote Sens.* **2022**, *14*, 2080. <https://doi.org/10.3390/rs14092080>

Academic Editors: Carmen Quintano, Alaitz Zabala Torres, Joan Masó and Ivette Serral

Received: 13 February 2022

Accepted: 21 April 2022

Published: 26 April 2022

**Publisher's Note:** MDPI stays neutral with regard to jurisdictional claims in published maps and institutional affiliations.



**Copyright:** © 2022 by the authors. Licensee MDPI, Basel, Switzerland. This article is an open access article distributed under the terms and conditions of the Creative Commons Attribution (CC BY) license (<https://creativecommons.org/licenses/by/4.0/>).

## 1. Introduction

The Amazon has been the world's most significant carbon sink from a global climate perspective. It is estimated to capture up to 25% of global carbon generation in plants and other biomass [1,2]. Thus, episodic and extensive biomass burning in the Amazon rainforest has led to severe local and even significant global effects, making the viability of the Amazon a global concern [3–5].

Human-driven deforestation of the forest has resulted in a major concern regarding the increasing wildfires, which are used to clear land for agriculture, livestock, mining, and lumber. Most forests are typically cleared using slash-and-burn processes; vast amounts of

biomass are removed by first pulling down the trees in the Amazon using bulldozers and giant tractors during the wet season, followed by torching the tree trunks several months later in the dry season [6,7]. Excessive growth in deforestation in 2019 seriously threatened this region [8,9]. Drier biomass, coupled with gradually rising ambient temperatures, was able to promote fire spread, ultimately resulting in the most robust fire event in the Amazon rainforest since 2013. The smoke from the fires darkened the city of São Paulo despite being thousands of kilometers from the Amazon [10]. As of 29 August 2019, more than 80,000 fires across Brazil had been reported, a 77% year-to-year increase for the same tracking period. Over 906,000 hectares of forest within the Amazon biome were lost to fires in this event [11].

The massive amount of smoke emitted from the Amazon rainforest results in very high concentrations of atmospheric particles, potentially contributing significantly to the excess carbonaceous content. Both absorption and scattering properties of these biomass aerosols influence the fluxes of radiation directly incident on the surface and to the top-of-atmosphere (TOA), and have significant impacts on global climate [12–14]. The monthly average direct radiative forcing of smoke from biomass burning in the Amazon region was reported to cause a negative direct radiative forcing during the dry season, varying from several to tens of  $\text{W m}^{-2}$  at the TOA and from  $-20$  to  $-70 \text{ W/m}^2$  at the surface [15,16]. Extensive investigations pointed out that the instantaneous effects of some extreme combustion events could be as high as  $-30 \text{ W/m}^2$  at the top of the atmosphere and  $-80 \text{ W/m}^2$  at the surface [17–19]. Significant changes in radiation can lead to spatial perturbations and redistribution of energy, triggering subsequent changes in the surface energy budget, surface–atmosphere flux exchange, atmospheric thermodynamic stability, and cloud evolution [14,20–23]. Over the past decades, an increasing number of studies have focused on obtaining additional aerosol parameters from satellite signals to enhance the knowledge of ambient aerosols [24–26]. However, the content of BC, an absorbing aerosol, has not been retrieved in the Amazon wildfire based on the satellite sensors, but probably plays a significant role in the radiative forcing of the wildfire smoke.

This paper characterizes the aerosol pollution during the 2019 Amazon wildfire from a satellite remote-sensing perspective and studies its direct radiative forcing impact by a comprehensive retrieval of different aerosol parameters. Here, a new aerosol retrieval algorithm was adopted to extend the moderate-resolution imaging spectroradiometer (MODIS) aerosol products [27]. The method was designed to estimate the black carbon (BC) aerosol concentration parameters from the MODIS aerosol optical depth (AOD) by taking full advantage of the high-quality products. It responds well to unexpected pollution events. It gives reasonable estimations of additional aerosol absorption parameters, such as single-scattering albedo (SSA), aerosol-absorption optical depth (AAOD), and BC volumetric fractions. Based on these satellite aerosol datasets, we deeply analyzed the noticeable changes and transport processes of each aerosol parameter before and after this intense event. We also compared the retrievals for 2019 to those from 2018 to better understand the impact of this severe pollution event, not only in terms of aerosol parameter changes, but more importantly, also in terms of direct radiative forcing effects on climate.

## 2. Materials and Methods

### 2.1. MODIS

#### 2.1.1. Operational MODIS Datasets

MODIS can monitor atmospheric pollution events on a daily scale [28]. This study adopted the daily Level 2 AOD from MODIS to establish extended aerosol datasets [25]. The measurements from the MODIS Terra satellite were used, as the overpassing time is approximately at 10:30 a.m. (local time) when cumulus clouds are weakly developed in the morning, and more valid pixels can be captured in the images [29]. MODIS-combined value-added AOD records with high-quality flags were selected, since they have excellent accuracy over bright and dark surfaces. The AOD retrieved for a wavelength of  $0.55 \mu\text{m}$  had a good comparison with the Aerosol Robotic Network (AERONET), within the expected

error of  $\pm(0.05 + 15\%)$  [25,30]. In addition, MODIS TOA reflectance data (MOD021KM) and a surface-reflectance estimation strategy (from the Collection 6 AOD algorithm) were also used. All satellite data were scaled to a spatial resolution of 10 km.

### 2.1.2. Algorithmic Framework for Estimating the Additional Aerosol Parameters

The framework of the algorithm is shown in Figure 1. The retrieval algorithm was developed based on the BC retrieval algorithm in our previous study [27]. The forward model was updated by coupling the mixing model to the satellite radiative transfer process. The aerosol composition was parameterized using a certain fraction of BC ( $f_{BC}$ ) and background aerosol properties (BA) instead of a simple after-mixing definition. Thus, the specific BC fractions could be retrieved over Lambertian surfaces depending on the forward simulation that best fit the TOA radiance signals of MODIS.

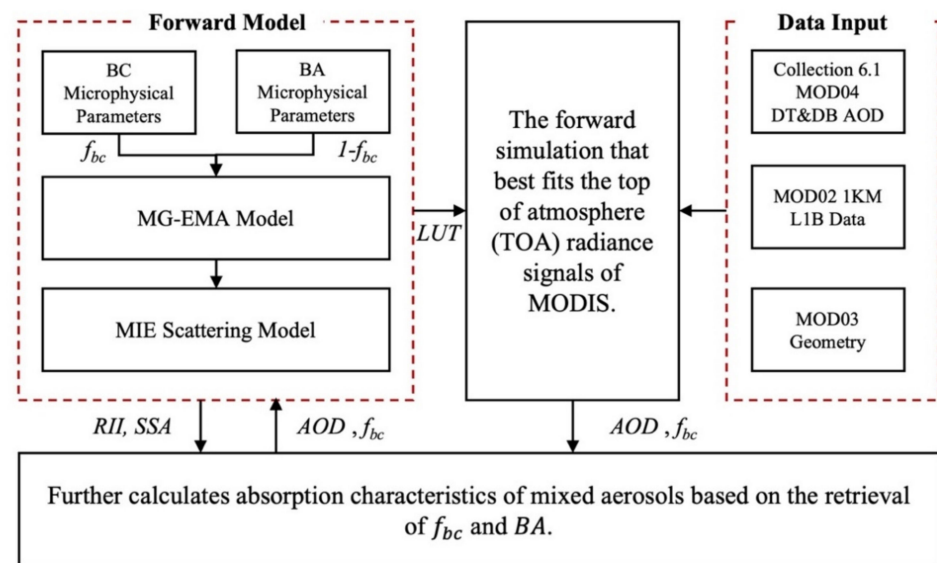


**Figure 1.** The algorithmic framework for estimating the BC content and additional aerosol absorption parameters from MODIS.

Additionally, some absorption characteristics of mixed aerosols can be further calculated based on the retrieval of  $f_{bc}$  and BA. Refractive indexes of an aerosol mixture ( $RI_M(\lambda)$ ), which is the square root of dielectric function ( $\epsilon_M(\lambda)$ ), can be calculated based on the Maxwell Garnett effective-medium approximation (MG-EMA) [31]:

$$\epsilon_M(\lambda) = \epsilon_{BA}(\lambda) \left[ 1 + \frac{3f_{BC} \left( \frac{\epsilon_{BC}(\lambda) - \epsilon_{BA}(\lambda)}{\epsilon_{BC}(\lambda) + 2\epsilon_{BA}(\lambda)} \right)}{1 - f_{BC} \left( \frac{\epsilon_{BC}(\lambda) - \epsilon_{BA}(\lambda)}{\epsilon_{BC}(\lambda) + 2\epsilon_{BA}(\lambda)} \right)} \right] \quad (1)$$

where  $\epsilon_{BC}(\lambda)$  is the effective dielectric function of black carbon at wavelength  $\lambda$ , and  $\epsilon_{BA}(\lambda)$  is the effective dielectric function of background aerosols at wavelength  $\lambda$ .

The volumetric size distribution (VSD) of aerosol compounds can be well described by the individual components of a mixture [32,33]:

$$\frac{dV(r)}{d \ln r} = \sum_{j=1}^n \frac{V_j(\tau)}{\sqrt{2\pi} \ln \sigma_j} \exp \left[ -\ln^2 \left( \frac{r}{r_{m,j}} \right) / 2(\sigma_j)^2 \right] \quad (2)$$

where  $V_j(\tau)$  is the volumetric concentration of components  $j$ ; and  $r_{m,j}$  and  $\sigma_j$  are the median radius and geometric standard deviation of lognormal distribution, respectively.

Finally, the spectral SSA ( $\omega$ ) of aerosols can be further simulated by inputting the *RI* and *VSD* retrievals into the MIE scattering model [34], and we therefore estimated the AAO ( $\tau_a$ ) using the following equation:

$$\tau_a = \tau(1 - \omega) \quad (3)$$

This algorithm has been tested and validated over China, and showed good agreements with ground-based observations.

In this study, the aerosol absorption was parameterized by detailing the microphysical parameters of BC and BAs, as well as their mixing states in the atmosphere, to retrieve the BC volume fraction from satellite images. The flowchart of the proposed algorithm is depicted in Figure 1.

### 2.1.3. Updating the Algorithm for the Amazon Rainforest Region

To apply the above framework for Amazonia, a reclustering of background aerosols (BA) was required, mainly because ambient aerosols in different regions were significantly influenced by regional surface types, emissions, and industrial structures, which are very different [32]. Therefore, in this study, we used AERONET inversion data (including information on SSA, RI, VSD) from 2015–2019 in the biomass burning season (July–September) of Amazonia for reclustering [35]. The strong scattering clusters were selected as the final BA model, since BC strongly absorbs solar radiation. Only one scattering aerosol model was recognized, while organics or dust, which are aerosols with weak absorptive characteristics, were not evident in Amazonia. The relevant microphysical parameters of BA are shown in Table 1.

**Table 1.** Clustered microphysical parameters of background aerosol.

	0.441 $\mu\text{m}$	0.674 $\mu\text{m}$	0.871 $\mu\text{m}$	1.02 $\mu\text{m}$
$n_{BA}$ <sup>1</sup>	1.462 $\pm$ 0.024	1.476 $\pm$ 0.014	1.484 $\pm$ 0.011	1.486 $\pm$ 0.009
$k_{BA}$ <sup>2</sup>	0.0052 $\pm$ 0.0033	0.0048 $\pm$ 0.0033	0.0052 $\pm$ 0.0033	0.0054 $\pm$ 0.0032
$\omega$	0.938 $\pm$ 0.010	0.927 $\pm$ 0.013	0.911 $\pm$ 0.016	0.907 $\pm$ 0.018
$r_{BA}$ <sup>3</sup> fine mode		0.547 $\pm$ 0.103		
$\sigma_{BA}$ <sup>4</sup> fine mode		0.422 $\pm$ 0.010		
$r_{BA}$ <sup>5</sup> coarse mode		3.117 $\pm$ 0.086		
$\sigma_{BA}$ <sup>6</sup> coarse mode		0.654 $\pm$ 0.018		

<sup>1</sup> Real parts of the refractive index (RI); <sup>2</sup> imaginary parts of the refractive index (RI); <sup>3</sup> radius of fine mode; <sup>4</sup> root-mean-square error of fine-mode radius; <sup>5</sup> radius of coarse mode; <sup>6</sup> root-mean-square error of coarse-mode radius.

In addition, for the microphysical parameters of BC monomers, we still adopted a wavelength-dependent RI ( $n_{BC} + k_{BC}i$ ) over the visible and near-visible wavelengths (Equation (4)) and a constant VSD ( $r_{BC} = 0.095 \mu\text{m}$  and  $\sigma_{BC} = 1.80 \mu\text{m}$ ) in the forward simulation [36,37]:

$$\begin{cases} n_{BC}(\lambda) = 1.811 + 0.1263 \ln \lambda + 0.027 \ln^2 \lambda + 0.0417 \ln^3 \lambda \\ k_{BC}(\lambda) = 0.5821 + 0.1213 \ln \lambda + 0.2309 \ln^2 \lambda - 0.01 \ln^3 \lambda \end{cases} \quad (4)$$

where  $n_{BC}(\lambda)$  and  $k_{BC}(\lambda)$  represent the real and imaginary parts of the refractive index (RI), respectively.

In the proposed algorithm, we assumed that the aerosol particles consisted of strongly absorbing BC and scattering background aerosols. Therefore, it was vital to remove the effects of BC in the clustering of background aerosol types. In our strategy, we performed a two-step operation. In the first step, since BC is a fine particle with strong absorption, we first removed all the strong absorption fine particles that may be affected by BC from the AERONET dataset to be clustered. The threshold values set here were  $\text{SSA}_{675} < 0.9$  and  $\text{FMF} > 0.4$ . In the second step, the processed dataset was clustered using the k-means model. We set 4 clusters here, and similar types were combined. Finally, the strongest scattering type was selected as the background aerosol. In this way, we could remove the effects of BC from the clusters. In fact, unlike China (where we tested in the previous

study), the background aerosol type in Amazonia was very homogeneous, so only one background aerosol could be obtained.

The relevant contents, and more a detailed description, including the algorithm procedure can be seen in the Supplementary Materials (Equations (S1) and (S2)).

## 2.2. AERONET

### 2.2.1. AERONET AOD and Inversions

In situ measurements are the primary means of discussing the accuracy of MODIS aerosol datasets. AERONET is a global network of ground-based instruments that compose an observing system to measure atmospheric aerosol properties. The system is equipped with a CIMEL Electronique 318A (CE-318) spectral radiometer that measures sun and sky radiances at several fixed wavelengths within the visible and near-infrared spectrum, providing continuous cloud-screened observations of spectral AOD and aerosol-inversion products (e.g., volume size distribution, aerosol complex refractive index, optical absorption, and the aerosol-scattering phase function) in different aerosol regimes [35].

All analyses in this study utilized the latest version 3.0 AERONET products outlined by Giles et al. (2019) [38]. Figure 2 flagged six low-altitude AERONET sites around the Amazonia basin that could have been affected by the 2018/2019 wildfires. A retrieval only reached Level 2.0 when the level of  $0.44 \mu\text{m}$  AOD was greater than 0.4, and other almucantar and hybrid quality checks were satisfied [39]. Thus, level 1.5 inversions were still used to increase the data available for analysis.



**Figure 2.** Low-altitude AERONET sites around Amazonia basin that could have been affected by the 2018/2019 wildfires.

### 2.2.2. Estimating the BC Volumetric Fractions from AERONET

For the BC content in the atmosphere, AERONET did not provide relevant records. It can usually be estimated using the absorbing parameters of AERONET inversions. In this study, the five-component (BC and other four weak/nonabsorbing components) inversion method proposed by Wang et al. (2013) [40] was used. This method could effectively reduce

the influence of weakly absorbing aerosols on BC retrievals by using the spectral SSA and RI acquired by AERONET inversions. The algorithm was implemented with the following cost function:

$$\chi^2 = \sum_{\lambda=1}^3 \frac{(n_{\lambda}^{cal} - n_{\lambda}^{obs})^2}{(n_{\lambda}^{obs})^2} + \sum_{\lambda=1}^3 \frac{(k_{\lambda}^{cal} - k_{\lambda}^{obs})^2}{(k_{\lambda}^{obs})^2} + \frac{(dSSA^{cal} - dSSA^{obs})^2}{|dSSA^{obs}|} \quad (5)$$

where the superscripts 'obs' and 'cal' represent the optical physical parameters of the mixed heterogeneous aerosol provided by AERONET inversions and mixing-model simulation, respectively. The modeled real ( $n_{\lambda}^{cal}$ ) and imaginary ( $k_{\lambda}^{cal}$ ) parts of the complex refractive index were simulated by MG-EMA (Equation (1));  $dSSA$  is the difference between  $SSA_{870}$  and  $SSA_{670}$ , which can be calculated as:

$$dSSA = \frac{\sum_{i=1}^3 MAE_i^{0.67} \rho_i f_i V_{total}}{\tau_{ext}^{0.67}} - \frac{\sum_{i=1}^3 MAE_i^{0.87} \rho_i f_i V_{total}}{\tau_{ext}^{0.87}} \quad (6)$$

where  $MAE_i^{\lambda}$  is the spectral mass absorption efficiency of components  $i$  at wavelength  $\lambda$   $\mu\text{m}$ ;  $\rho_i$  and  $f_i$  are the density and volumetric fractions of components  $i$ , respectively;  $V_{total}$  is the total aerosol volume concentration; and  $\tau_{ext}^{\lambda}$  is the extinction AOD at wavelength  $\lambda$   $\mu\text{m}$ . The parameters of each component in the equation can be found in Supplementary Materials Table S2.

### 2.3. Direct Radiative Forcing Simulation

In this study, the direct radiative forcing of the aerosols emitted from the pollution event was simulated using the Santa Barbara DISORT Atmospheric Radiative Transfer (SBDART) model [41], which is a tested and reliable physical model developed by the atmospheric science community over decades. As mentioned above, the satellite inversion results were reliable for the high-pollution scenarios. Although the uncertainty was relatively high at a lower AOD, this did not affect the later conclusions regarding radiative forcing, since low aerosol concentrations in the radiation were almost negligible, regardless of the aerosol particles' scattering and absorption strengths. The model was operated with 33 height layers and four radiative streams, and the direct radiative forcing of aerosols (ARF) at TOA/surface levels could be calculated from the simulated up ( $F^{\uparrow}$ )/down ( $F^{\downarrow}$ ) radiative flux:

$$ARF = (F^{\downarrow} - F^{\uparrow})_{aerosol} - (F^{\downarrow} - F^{\uparrow})_{pristine} \quad (7)$$

where the subscripts 'aerosol' and 'pristine' represent the radiative flux with and without aerosols, respectively. It was necessary to simulate the ARF at the TOA ( $ARF_{TOA}$ ) and surface levels ( $ARF_{SRF}$ ), respectively, from which the atmosphere aerosol radiative forcing ( $ARF_{ATM}$ ) could be further deduced:

$$ARF_{ATM} = ARF_{TOA} - ARF_{SRF} \quad (8)$$

Here, the MODIS aerosol dataset we retrieved provided AOD and SSA inputs required for SBDART. Another required asymmetry factor was not a direct output in the algorithm, but it could be obtained by MIE simulations based on the recomputed complex refractive indexes and size distributions (Equations (1) and (2)).

## 3. Results

### 3.1. Comparing Satellite Aerosol Datasets with AERONET

Figure 3 shows the comparison of the AOD (0.55  $\mu\text{m}$ ), SSA (0.55  $\mu\text{m}$ ), AAOD (0.55  $\mu\text{m}$ ), and BC volumetric fractions ( $f_{bc}$ ) obtained from MODIS with the ground-based AERONET records. The points in Figure 3 are the matched records for 30 min before and after the overpass time of MODIS, corresponding to the  $5 \times 5$  pixels over the stations. The matchup

criterion was to have at least 2/3 of the pixels from valid MODIS retrievals within a window surrounding the AERONET site.

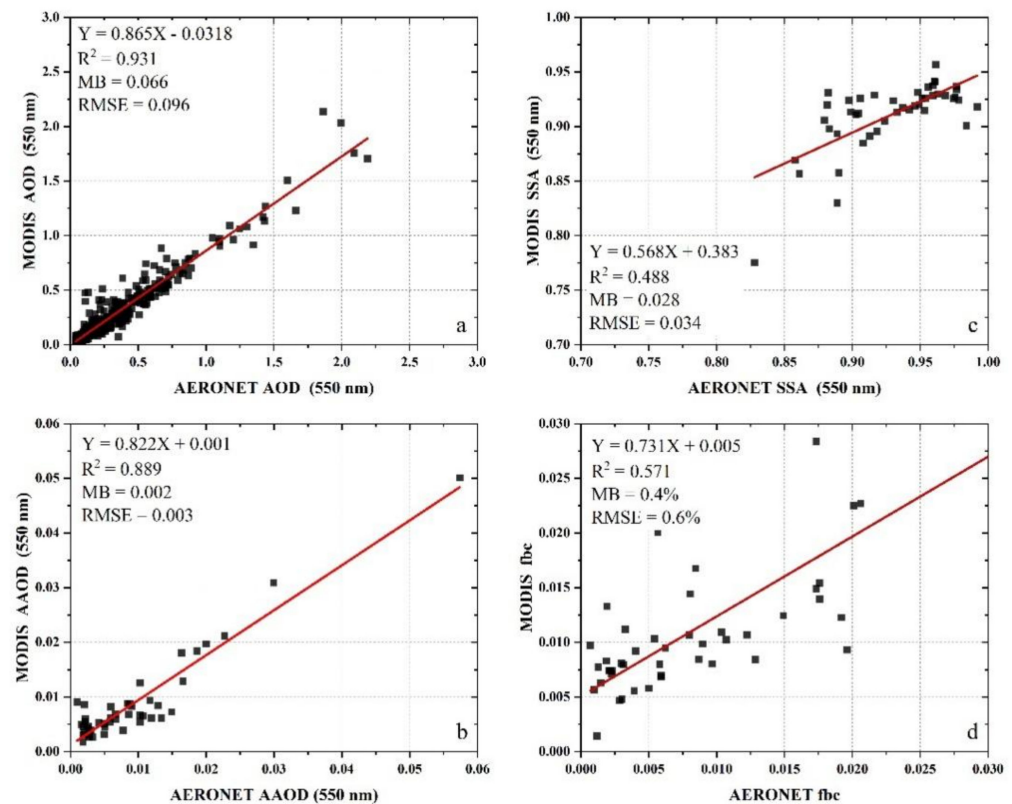


**Figure 3.** The comparison of the MODIS aerosol datasets used in this study with the ground-based AERONET records: (a) AOD (0.55  $\mu\text{m}$ ); (b) SSA (0.55  $\mu\text{m}$ ); (c) AAOD (0.55  $\mu\text{m}$ ); (d) BC volumetric fractions ( $f_{bc}$ ).

Figure 3 shows different quantities of the AOD and other products. The main reason was that AERONET provided AOD and SSA from two different products (AOD from the Aerosol Optical Depth Datasets and SSA from the Aerosol Inversion Datasets). The records for the AOD are much more numerous than those of the SSA. This was attributed to the limitations of the AERONET inversion algorithm. Only those results that can converge in the model are published. At the same time, the bad inversions are excluded from the datasets. Furthermore, such inversion data reaches Level 2.0 only when the level of 0.44  $\mu\text{m}$  AOD is more significant than 0.4 and other almucantars, and the hybrid quality check is satisfied. Thus, it is inevitable that the number of points in the AOD will be different from those for the SSA.

The MODIS AOD demonstrated a high level of accuracy (Figure 3a). The correlation coefficient ( $R^2$ ) with AERONET reached 0.931, with a mean error (MB) of only 0.066 and a root mean square error (RMSE) of less than 0.1. Although an overall underestimation was present, the MODIS AOD could easily be revised by a simple linear equation. In contrast, the correlation between the MODIS SSA and AERONET inverted SSA appeared to be lower ( $R^2 = 0.488$ ) due to the uncertainty of the algorithm itself [27]. Thus, it was difficult to revise satellite SSA by a simple linear function, such as the AOD. However, the error indicators exhibited essentially the same levels as the uncertainty of the AERONET SSA (<0.03 when AOD > 0.5), with a low MB of 0.028 and a low RMSE of 0.034. The low bias of the AOD and SSA also made the MODIS AAOD very reasonable (Figure 3c), with an  $R^2$  of 0.889, MB of 0.002, and RMSE of 0.003. The BC volumetric fractions obtained by the MODIS algorithm were compared with those retrieved using the AERONET method (Figure 3d). The correlation coefficient was found to be 0.571, with an MB of 0.4% and an RMSE of 0.6%.

In summary, the MODIS aerosol datasets produced by the updated algorithm could provide full-coverage and reliable data over specific time periods, and provided further details on biomass-burning aerosols in the Amazonia.

Our previous study revealed the main factors (i.e., AOD inputs, the surface-reflectance hypothesis, and the variances in the background models for non-BC aerosols) that contributed to the model errors. A summary of the uncertainty analyses for each factor contributing to the model errors of primary retrieval in our algorithm (volume fraction of BC) and a more detailed analysis of the errors can be found in the Supplementary Materials S2. The uncertainty analyses for each factor are shown in Table S1.

### 3.2. Absorbing Aerosols Emitted during the 2019 Amazon Wildfire

Many studies have confirmed that the violent combustion of biomass simultaneously releases large amounts of carbonaceous aerosols [42,43]. The smoke strongly absorbs solar radiation, further affects the radiation balance, and deteriorates the climate in the long term [44,45]. Figure 4 demonstrates a satellite image of the Amazon wildfire for 17 August 2019 (one day selected from this biomass burning event), which was remotely sensed by using updated aerosol-detection algorithms and thermal anomalies detected by MODIS satellites.

Figure 4a shows the MODIS RGB images of the study region and time. The wind-borne anomalous plumes of smoke formed from the Amazon rainforest to the territory of Paraguay, and the southern rainforest was especially covered with heavy smoke that obscured the surface information from the space view. Using the fire and thermal-anomaly detection algorithm of MODIS [46], a large number and density of fire counts from high-temperature biomass burning were simultaneously identified near these smoke plumes. Note that the firing density was very low in pristine forests, while about 60–70% of all MODIS-measured fire anomalies were located at the junction of artificial land that expanded into the rainforest (Figure 4b). The results implied that the wildfires and the severe pollution smoke in the Amazon rainforest may have been attributable to the human-driven deforestation of the Amazon rainforest.

The AOD distribution at 0.550  $\mu\text{m}$  (Figure 4c) showed that the AOD of dense smoke could reach 1.0 or even higher. For a region with a homogeneous climate environment such as the Amazon rainforest, the magnitude of AOD in a daily variation also represented the level of air pollution. These smoke plumes thus implied localized air pollution with significant aerosol optical forcing. In addition, it can be seen that most high values for the absorbing aerosol optical depth (AAOD > 0.1) in the study area were consistent with the spatial distribution of the AOD (Figure 4d–f). These high values were attributed to the strong absorbing BC in the atmosphere (Figure 4e). Usually, the volumetric fractions of strongly absorbing BC in an aerosol compound introduced a very significant effect on the absorption capacity of mixed heterogeneous aerosols, driving a shift from strongly scattering aerosols (SSA > 0.95) to strongly absorbing aerosols (SSA < 0.90).

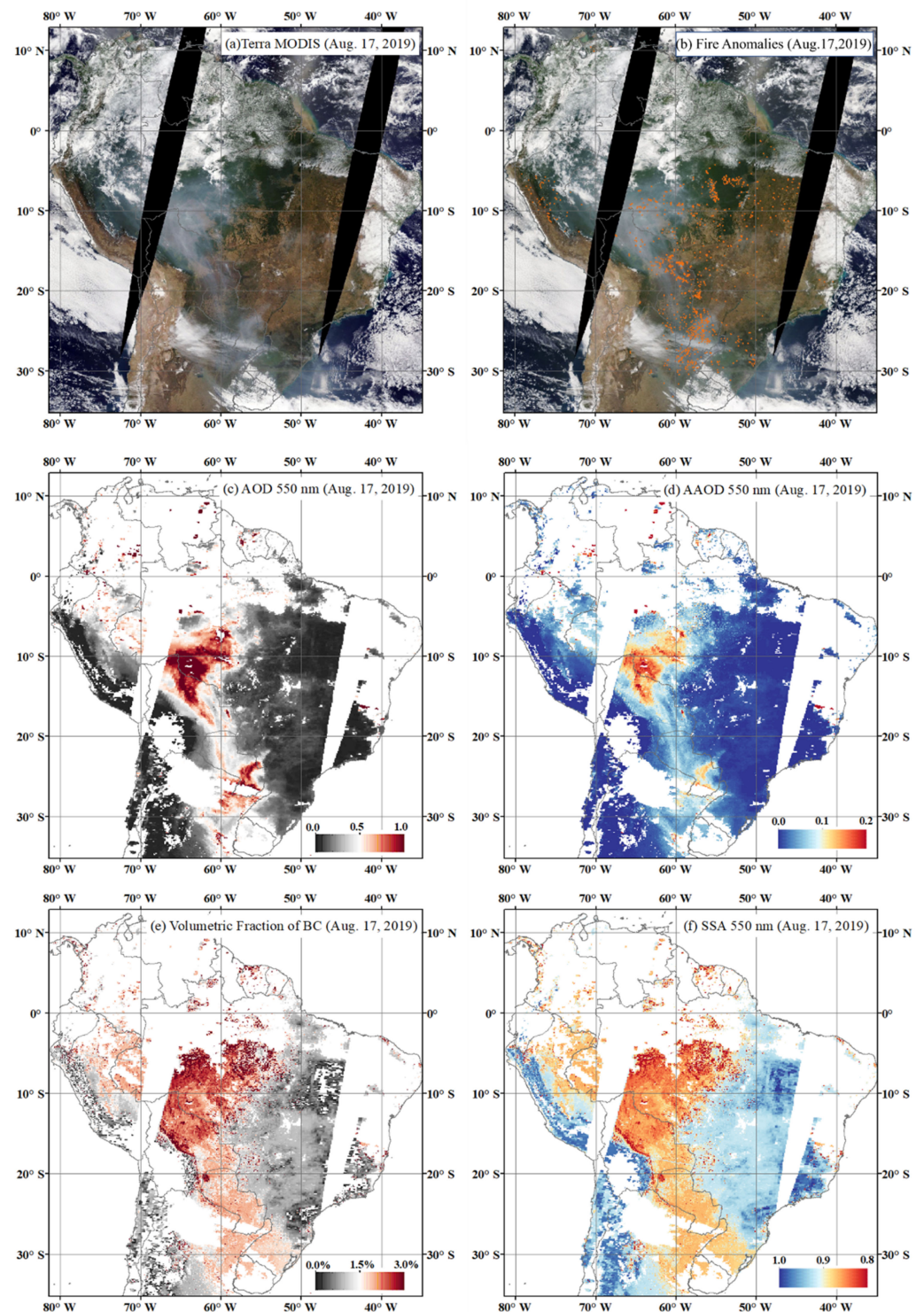


**Figure 4.** Satellite monitoring of Amazon wildfire for 17 August 2019: (a) MODIS Terra RGB image showing the biomass burning event over the Amazon; (b) MODIS fire and thermal-anomaly counts; (c) retrievals of MODIS AOD ( $0.55 \mu\text{m}$ ); (d) AAOD ( $0.55 \mu\text{m}$ ) retrieved by the proposed algorithm; (e)  $f_{bc}$  retrieved by the proposed algorithm; (f) SSA ( $0.55 \mu\text{m}$ ) retrieved by the proposed algorithm.

#### 4. Discussion

##### 4.1. Variations in Aerosol Properties during the Transport of Polluted Air Masses

Atmospheric pollutants undergo regional and intercontinental transport to remote areas at properties much different from the sources. In particular, for BC aerosols emitted

from biomass burning, the shorter lifetime (a few days to weeks) and the aging process often lead to changes in aerosol properties during the regional transport of polluted air masses [45].

Figure 5a shows the RGB image for 22 August 2019 (day of year (DOY) = 234, another day at the height of this event) from MODIS TERRA, overlaying the results of the forward trajectory from one week earlier (15 August 2019, DOY = 227). The forward trajectories and the above-ground level (Figure 5b) were simulated using the Hybrid Single-Particle Lagrangian Integrated Trajectory (HYSPLIT) model. This widely used model can simulate air-mass transport trajectories from a given meteorological dataset at different altitudes and times [47]. The forward trajectory simulation began from the location of the fire-hit area on the border between Brazil, Peru, and Bolivia. In this case, the trajectory of the air masses beginning on 15 August matched well with the distribution of the smoke after seven days.

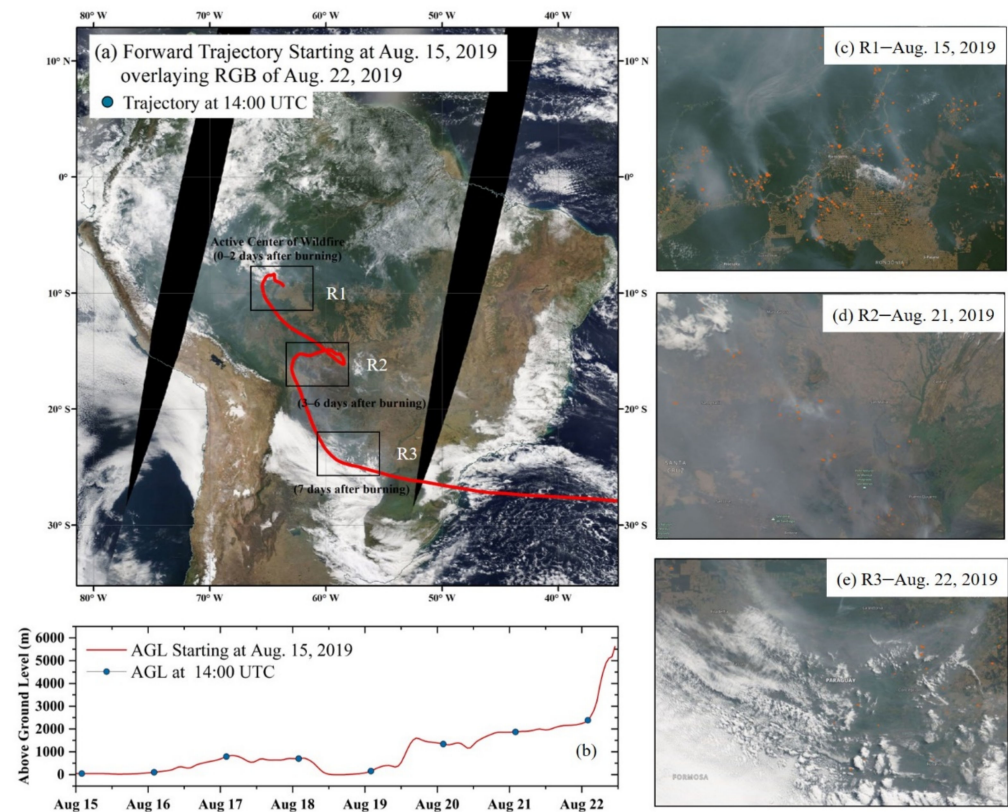


**Figure 5.** (a) RGB image for 22 August 2019 (DOY = 234) from MODIS TERRA, overlaying the results of the HYSPLIT forward trajectory from one week earlier (15 August 2019, DOY = 227). (b) Above-ground level (ABL) from HYSPLIT forward-trajectory simulation in (a). The location of the air mass at the time of satellite imaging (14:00 UTC) is marked with blue dots. Three subregions were selected based on the trajectory's locations and times, respectively influenced by local rainforest aerosol emissions, transported rainforest aerosols with other local emissions, and transported rainforest aerosols without other local emissions. The RGBs and anomalous fire count corresponding to the selected time is magnified in (c–e).

The region was divided into three subblocks according to the marked location of the air mass at the overpass time of the satellite (14:00 LT). Region R1 had a high fire density, indicating that local emission sources dominated the heavy smoke. Small trajectory changes (Figure 5b) within the entire boundary layer during the first 0–2 days of fire contributed to the accumulation of pollutants (magnified in Figure 5c). Afterward, the air mass carrying pollutants reached region R2 after a long-distance transport (magnified in Figure 5d). Transmitted rainforest-burning aerosols affected the area, along with the local emissions. High-level aerosol loadings could also be explained via stable air conditions (a slight change

in the trajectory). Region R3 was the position of the air mass one week after the rainforest source emission (magnified in Figure 5e). Almost no active anomalous fire counts were identified (Figure 5e), indicating that the contamination was mainly dominated by external sources. Additionally, the air-mass dynamics were powerful in R3; the polluted air mass rapidly spread to the ocean and rose to more than 2 km vertically. The characteristics of the three subregions are summarized in Table 2.

**Table 2.** Characteristics of the three subregions.

Region	Sources	Trajectory Changes
R1	Local emission	Weak
R2	Local emission and transmitted aerosols	Weak
R3	Transmitted aerosols	Strong

Figure 6 shows the daily variations in the MODIS aerosol retrievals over these subregions throughout the entire pollution event (July to September 2019). The changes in aerosol properties before and during the event are summarized in Table 3. The retrievals with more than 50% cloud coverage were ignored. Considering that the Amazon has a low AOD without active biomass-burning activities, a threshold of 0.5 was applied, and the region was affected by this severe event when the AOD was  $>0.5$  consistently or repeatedly. The results showed that the beginning of contamination detected in each of the three subregions differed in time (corresponding to DOY = 215, 219, and 220, respectively). They were consistent with the forward trajectory, as previously mentioned.

**Table 3.** Changes in aerosol properties of the three selected subregions before and during the event in Amazonia (before event  $\rightarrow$  during event).

Region	AOD (0.55 $\mu\text{m}$ )	AAOD (0.55 $\mu\text{m}$ )	SSA (0.55 $\mu\text{m}$ )	$f_{bc}$
R1	0.211 $\rightarrow$ 0.794	0.020 $\rightarrow$ 0.090	0.913 $\rightarrow$ 0.887	0.010 $\rightarrow$ 0.016
R2	0.170 $\rightarrow$ 0.661	0.012 $\rightarrow$ 0.072	0.931 $\rightarrow$ 0.897	0.007 $\rightarrow$ 0.014
R3	0.177 $\rightarrow$ 0.438	0.019 $\rightarrow$ 0.043	0.933 $\rightarrow$ 0.910	0.006 $\rightarrow$ 0.011

Before the event, all the aerosol parameters were at low levels. It is worth noting that the SSAs (0.55  $\mu\text{m}$ ) in R2 and R3 were very close to the background aerosols we clustered (SSA of BA $\sim$ 0.932). In contrast, the aerosol absorption characteristics were stronger in R1, even in the absence of extensive pollution, which was attributed to the perennially active biomass burning in R1. When the pollution event occurred, the comparison suggested significant changes in both aerosol loadings and absorption. The three subregions showed more than double or triple changes in the AOD at 0.55  $\mu\text{m}$  wavelengths before and during the event. The BC content in the atmosphere consequently increased due to the evident polluted air masses, with an increase of 50–100%. A significant increase in BC allowed the mixed aerosol to change from scattering to absorbing, as shown by a decrease in the SSA (0.55  $\mu\text{m}$ ) and a significant increase in the AAOD (0.55  $\mu\text{m}$ ). The variation in BC content was most significant in region R2, which was related to its presence in both local emissions and transmitted BC from R1.

#### 4.2. Year-to-Year Comparison of the Same Periods in 2018 and 2019

The 2019 wildfires in Amazonia were among the worst events in recent years, with 85% increased fire counts in Brazil compared to the same period in 2018, with more than half of the fires were in Amazonia [48]. Figures 7 and 8 show the Amazonian spatial distribution and daily variations of the four retrieved aerosol parameters in these two selected years. The retrievals allowed us to identify some significant year-to-year differences from July through September. According to the certain increase in wildfire events [49], we recognized DOYs 200 to 250 as the wildfire period of this event.

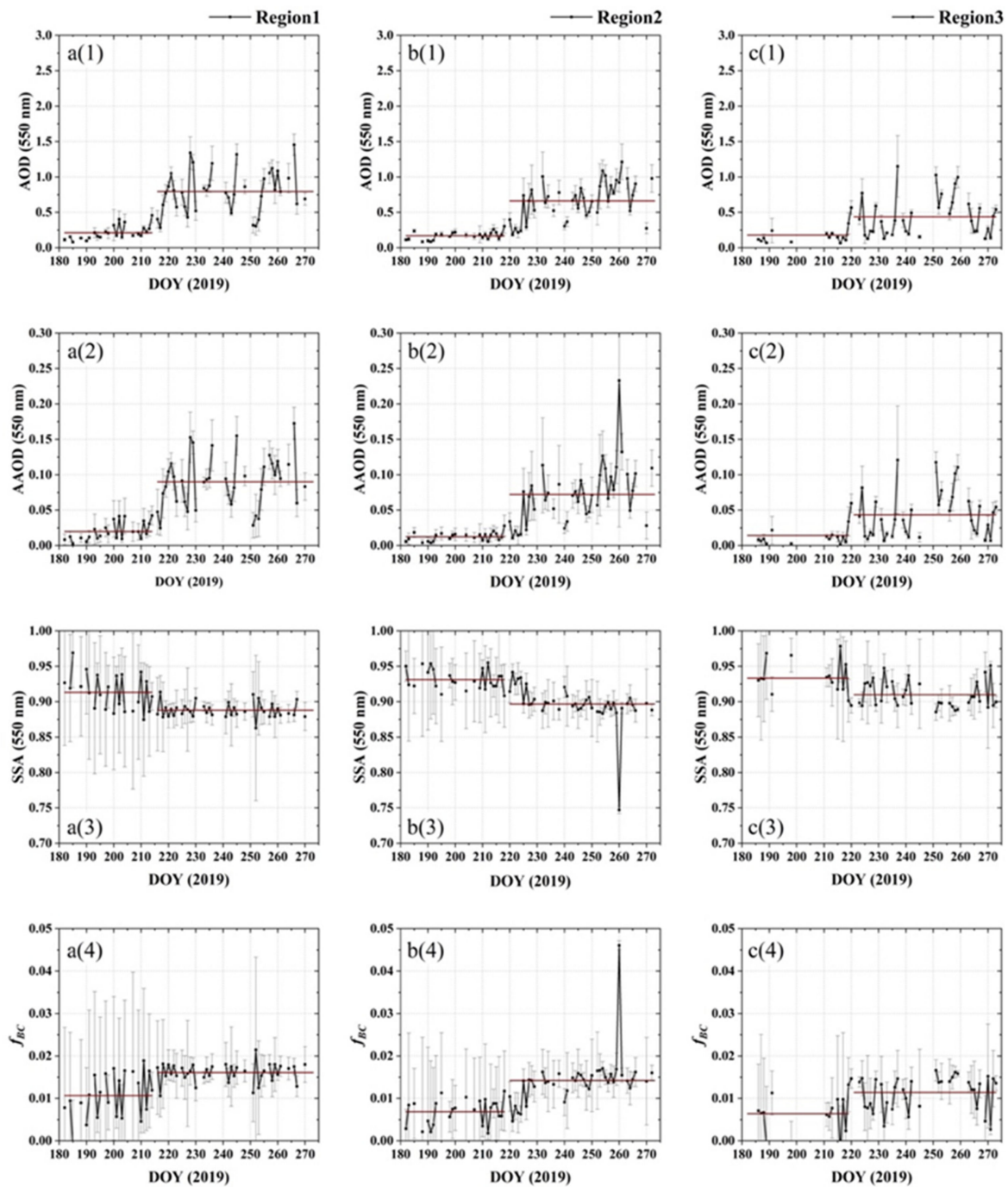


**Figure 6.** Daily variations in the MODIS aerosol retrievals over the three selected subregions shown in Figure 5 throughout the entire pollution event in Amazonia (July to September 2019). (a1–a4) AOD at 0.55  $\mu\text{m}$ , AAOD at 0.55  $\mu\text{m}$ , SSA at 0.55  $\mu\text{m}$ , and BC volumetric fractions ( $f_{bc}$ ) over region R1. (b1–b4) Retrievals over region R2. (c1–c4) Retrievals over region R3.

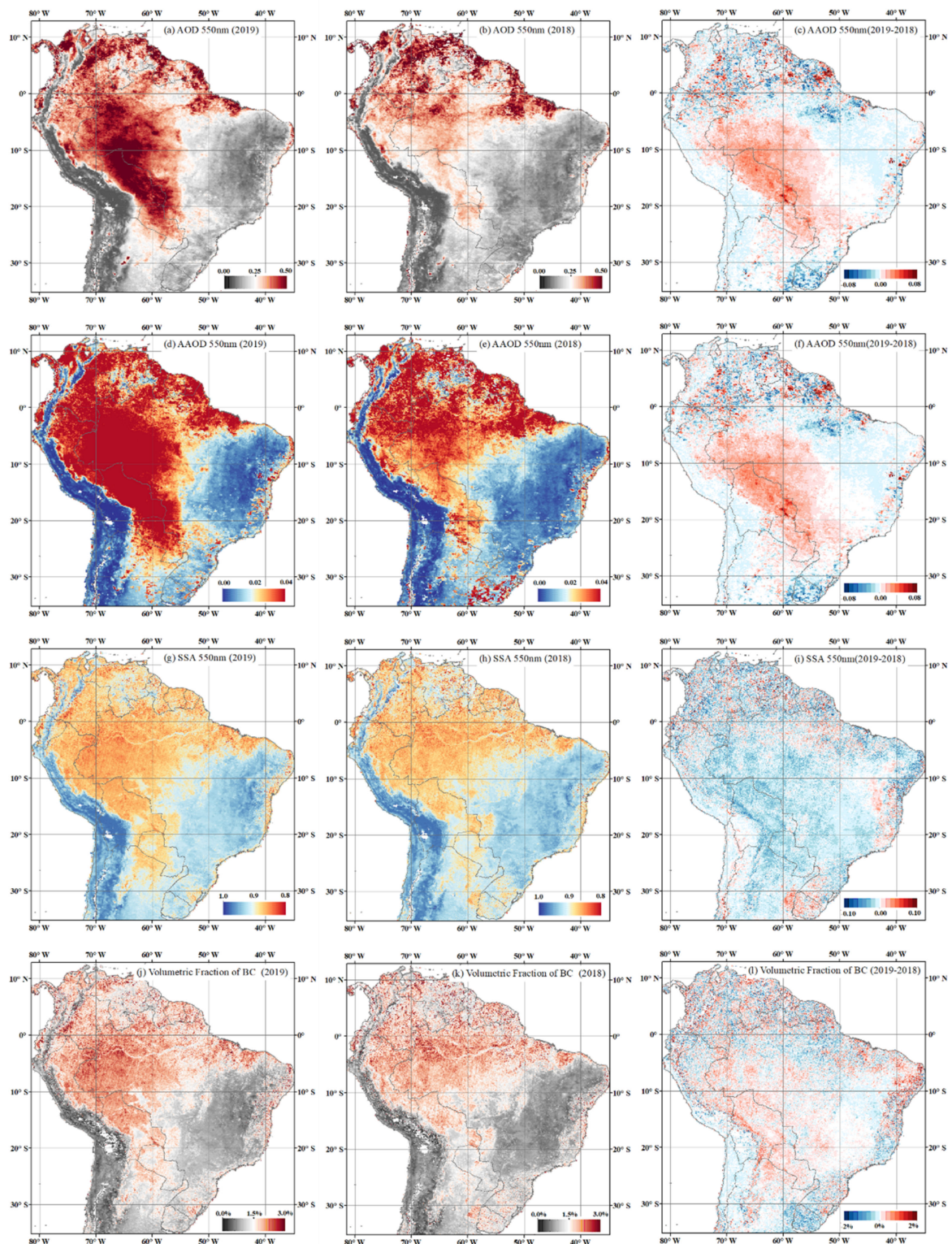


**Figure 7.** Averaged MODIS aerosol retrievals of Amazonia from July through September. The columns from left to right are for the results of 2019, 2018, and year-to-year differences, respectively. The rows from top to bottom represent AOD at 0.55 μm, AAOD at 0.55 μm, SSA at 0.55 μm, and BC volumetric fractions ( $f_{bc}$ ).

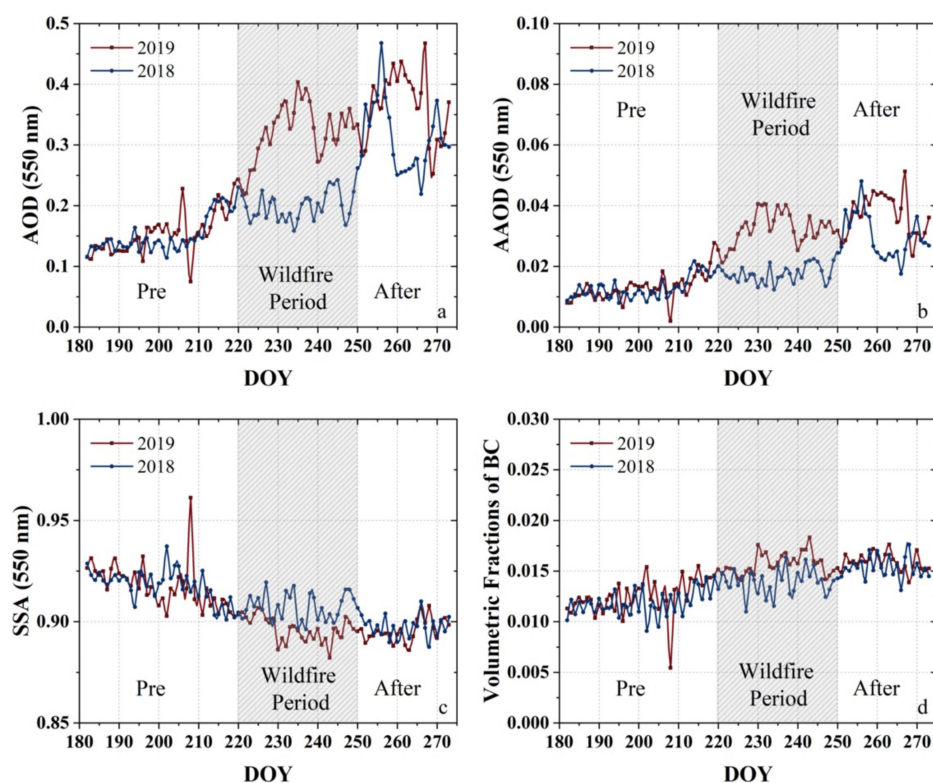


**Figure 8.** Daily variations in the MODIS aerosol retrievals for South America from July through September in 2018 and 2019: (a) AOD at  $0.55 \mu\text{m}$ ; (b) AAOD at  $0.55 \mu\text{m}$ ; (c) SSA at  $0.55 \mu\text{m}$ ; (d) BC volumetric fractions ( $f_{bc}$ ). The shading represents the peak of this event.

As shown in Figure 8, prior to the wildfire period ( $\text{DOY} < 220$ ), the aerosol retrievals did not differ significantly between 2018 and 2019. Although fluctuations could be recognized due to occasional biomass-burning events or meteorology, these parameters were kept at deficient levels. The AOD at  $0.55 \mu\text{m}$  was less than 0.2, the AAOD at  $0.55 \mu\text{m}$  did not exceed 0.02, the SSA at  $0.55 \mu\text{m}$  was greater than 0.90 and exhibited stronger scattering characteristics, and the BC with a volume fraction was less than 1.5%.

During the wildfire period ( $220 \leq \text{DOY} \leq 250$ ) the differentiation of the parameters in 2019 and 2018 gradually emerged. The spatial distribution showed a clear pattern of the changes, extending from the source (fire-hit area on the border between Brazil, Peru, and Bolivia) southeastward to the border between Paraguay and Argentina. The enhancements in the AOD and AAOD at  $0.55 \mu\text{m}$  were more pronounced than others during this continuous event, with a 150% increase in the AOD and a 200% increase in the AAOD compared to the same period in 2018. A small change in the absorption and BC content could also be identified, with a change in aerosol toward absorbing compounds (SSA at  $0.55 \mu\text{m} < 0.9$ ), and more BC being emitted ( $f_{bc}$  close to 2%).

After the wildfire period ( $\text{DOY} > 250$ ), the AOD and AAOD at  $0.55 \mu\text{m}$  in 2019 remained high and even elevated slightly. In contrast, the aerosol absorption and BC composition did not rise as steeply as the AOD and AAOD did. This indicated that although the air pollution from the wildfire events was still affecting the region, the new generation of strongly absorbing BC particles from emission sources was under control, with evidence that the volume fractions of BC in an aerosol particle were not further increased, since previously emitted biomass BC could be thinly or partially encapsulated and further coated with other materials. In addition, although two severe pollution events also occurred in 2018 (near  $\text{DOY} = 250$  and  $\text{DOY} = 270$ ), a speedy dissipation process can be identified, and the retrievals returned to pre-event levels within very few days. This suggested that such occasional and effectively controlled events did not affect the region in

the long term. In contrast, the earlier start and continuous burning in 2019 resulted in a longer-range, longer-lasting, and widespread pollution event.

#### 4.3. Direct Radiative Forcing Enhanced by the 2019 Amazonian Wildfire

Unnaturally emitted aerosol particles significantly impact global and regional climate through direct radiative forcing [45]. Such a severe air pollution event over Amazonia is bound to predict and significantly affect radiative balance.

Figure 9 shows the ARF calculations for aerosols (mixture of non-BC background aerosols with embedded BC particles) produced during the 2019 Amazon fires (July–September); the distribution shown in Figure 9 was obtained by averaging the ARF values across South America. Thus, the range in the values corresponded to the temporal variations throughout the entire duration of the contamination event. The results demonstrated the negative radiative forcing at the TOA and surface levels, with mean values of  $-12 \text{ W/m}^2$  and  $-38 \text{ W/m}^2$  during the entire event, respectively, which confirmed the cooling effect of the aerosol. ARF varied between different studies due to uncertainties associated with different scales and approaches. However, the magnitudes of the ARF values proposed in our study were within a reasonable range, and were similar to those for previous years when severe fires occurred in the dry season (Table 4).

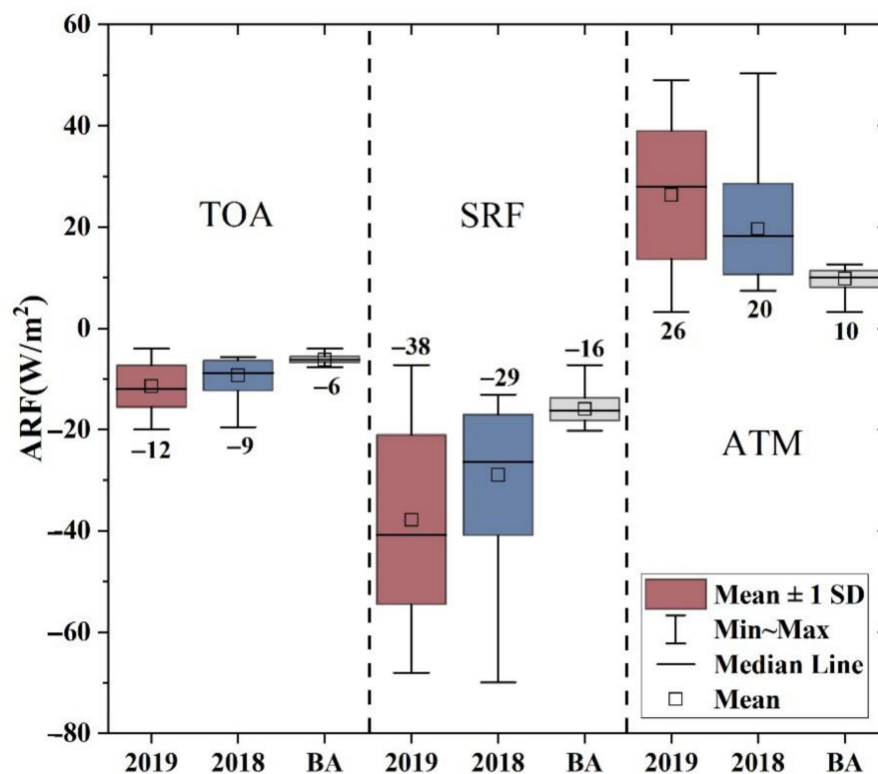


**Figure 9.** Aerosol radiative forcing during 2019 wildfire event (July–September), during the same period in 2018, and when the region was free from strong absorbing BC (pure background aerosol (BA) with  $\text{AOD}_{0.55\mu\text{m}} < 0.2$  and  $\text{SSA}_{0.55\mu\text{m}} > 0.92$ ). ARF at the TOA, surface, and in the atmosphere were simulated by the SBDART.

Compared with the ARF when the region was free from strong absorbing BC (pure background aerosol with  $\text{AOD}_{0.55\mu\text{m}} < 0.2$  and  $\text{SSA}_{0.55\mu\text{m}} > 0.92$ ), the 2019 event exhibited a more than 2-fold enhancement, with changes of  $-6 \text{ W/m}^2$  and  $-22 \text{ W/m}^2$  at the TOA and surface levels, respectively. The cooling effect represented 33% and 31% increases, respectively, compared to the impact of biomass-burning activities during the same period in 2018 ( $\text{ARF}_{\text{TOA}} = -9 \text{ W/m}^2$ ,  $\text{ARF}_{\text{SRF}} = -29 \text{ W/m}^2$ ). In contrast, it seemed that the 2019 wildfire emissions generated a more significant heating effect in the atmospheric column.

The ARF in the atmosphere was  $+26 \text{ W/m}^2$ , an increase of  $16 \text{ W/m}^2$  (160%) compared to the pure background aerosol cases and of  $6 \text{ W/m}^2$  (30%) compared to the same period in 2018. Higher ARF in the atmosphere was apparently caused by BC aerosols, which not only heated the atmosphere through strong absorption, but also simultaneously reduced the radiation reaching the TOA and surface levels.

**Table 4.** Dry-season radiative forcing ( $\text{W/m}^2$ ) at the TOA, at the surface, and in the atmosphere over the Amazonian region proposed in previous studies and in this study.

Reference	$ARF_{TOA}$	$ARF_{SRF}$	$ARF_{ATM}$	Data
Procopio et al. (2004) [15]	−5~−12	−21~−74	16~62	1993~2002, 2 sites
Sena et al. (2013) [50]	−4~−11	/	/	2000~2009, satellite retrievals
Sena and Artaxo (2015) [19]	−1~−9	/	/	2000~2009, satellite retrievals
Palacios et al. (2020) [18]	/	−41	/	2000~2017, 9 sites
This study	−12 (−4~−20)	−38 (−9~−70)	26 (3~50)	2019, satellite retrievals

Recently, there has been an increasing awareness that BC has measurable effects on atmospheric and land surface temperatures, primarily through radiative scattering and absorption in the atmosphere and systematic albedo changes at surfaces. These two effects make BC a strong driver of climate change from local to global scales [51,52].

For surface albedo, the events in 2019 provided a solid negative forcing at the surface ( $-38 \text{ W/m}^2$ ) by absorbing and blocking direct solar radiation, which directly led to the darkening of the surface. This effect, in turn, may have reduced the evaporation and rainfall over the region [53], and a drier environment is more likely to lead to frequent fires and trapped in a cycle of deterioration. Atmospheric heating (positive radiative forcing,  $+26 \text{ W/m}^2$ ) can directly exacerbate the warming process and curb the thermoregulatory capacity of the rainforest itself [54,55], especially for such vital pollution events. In addition, the heating of the atmosphere can increase the thermodynamic stability of the atmosphere and cause a decrease in precipitation, which not conducive to the diffusion of pollutants [56]. This makes it easier for these strongly absorbing particles to be deposited on the land and ocean surfaces, forcing a longer-term influence on these surfaces.

Therefore, these radiation-related effects of absorbing aerosol in the long-lasting, widespread wildfire events may accelerate the deterioration cycle of drought and fire. Brazil was reported to have suffered the worst drought in the two years following 2019 [57,58]. The feedback effect of excessive anthropogenic burning of trees in 2019 on the extreme drought climate in the Amazon from 2020 to 2021 is worthy of further investigations in the future.

## 5. Conclusions

The characteristics of the severe smoke emitted during the extreme biomass-burning events in the Amazon rainforest from July to September 2019 were studied through the MODIS aerosol retrievals. Analyses of the retrieved total AOD, as well as the absorption properties (SSA, AAOD, and BC content) were presented, and the major findings are given below:

- 1 The aerosol dataset was established based on our previously proposed algorithm [27] for BC estimation, which took advantage of the high-quality MODIS AOD dataset and estimated the proportion of BC components in the smoke by refining the mixing states of BC and non-BC aerosols. For the extremely high biomass-burning event in the Amazon rainforest, we further calculated the spectral SSA and AAOD of the smoke plumes using MG-EMA and an MIE scattering model. The new aerosol dataset allowed for more robust aerosol monitoring than would have been possible with the previously available aerosol database for polar-orbiting satellites;

- 2 To make the algorithm usable in Amazonia, we updated the ambient aerosol micro-physical features (non-strongly absorbing BC) by clustering the AERONET records over the region, which were updated and used as an input of the retrieval algorithm. The validation showed that the MODIS aerosol dataset was in good agreement with the data from the AERONET distributed in and around the rainforest. With the help of the high-quality MODIS AOD, the MODIS retrievals for AAOD, SSA, and BC exhibited low biases compared to the AERONET inversions (Level 2.0). Such satellite datasets with more parameters and full coverage are of great importance in detecting pollution processes, radiative-forcing estimation, and simulation of environmental climate effects for major events;
- 3 At the peak of this pollution event, the distribution of thick smoke with a high AOD and high absorption characteristics was very similar to anomalous fire counts. The AOD peaked above 1.0, emitting a large amount of BC (>3%) at the source. These particles simultaneously led to a very strong absorption, with  $SSA_{0.55\mu m} < 0.85$  and  $AAOD_{0.55\mu m} > 0.1$ . In addition, we successively selected three subregions for full-time monitoring based on the air-mass trajectories simulated by HYSPLIT. Significant enhancements in various aerosol properties were found during the pollution event. However, significant differences in the first detection, the duration, and the level of detected pollution could be recognized in the three selected regions due to the distance from the emission source, BC aging, and dynamics conditions. Accurately acquiring the changes and trends of the entire pollution event is important for studying the aging of aerosol particles from strong emission events;
- 4 The year-to-year comparison with 2018 showed that the 2019 Amazon rainforest wildfire visually showed a significant enhancement in the aerosol properties. The map-averaged  $AOD_{0.55\mu m}$  increased by 150%, and the  $AAOD_{0.55\mu m}$  by 200%, at the pollution peak. Small changes in absorption and BC content were also found, with more BC being emitted (map-averaged  $f_{bc}$  close to 2%), causing the aerosol to change toward absorbing compounds (map-averaged  $SSA_{0.55\mu m} < 0.9$ ). These enhancements continued to deteriorate the atmospheric environment over the Amazon rainforest and even all of South America;
- 5 Further simulations of the ARF showed that the massive absorption emitted during the 2019 Amazon fires forced a change in the radiative balance, which not only produced a more significant heating effect on the atmospheric column through solid absorption, but also reduced the radiation reaching the TOA and surface levels at the same time. The mean values of negative radiative forcing at the TOA and surface levels were  $-12 \text{ W/m}^2$  and  $-38 \text{ W/m}^2$ , respectively, and thus the ARF in the atmosphere was  $+26 \text{ W/m}^2$ . All three ARF indicators increased by  $\sim 30\%$  compared to 2018, and more than doubled compared to the pure background aerosol environment over the Amazonia, which may accelerate the deterioration cycle of drought and fire, most likely by reducing the rainfall due to the cooling surface and enhanced thermodynamic stability of atmosphere due to the atmospheric heating effect.

**Supplementary Materials:** The following supporting information can be downloaded at: <https://www.mdpi.com/article/10.3390/rs14092080/s1>, Equations (S1) and (S2); Table S1: Uncertainties of the algorithm under different AODs ( $\tau$ ); Table S2: The parameters used in the aerosol components retrievals from AERONET.

**Author Contributions:** Conceptualization, Y.L. and F.B.; methodology, S.Y. and F.B.; software, S.Y. and F.B.; validation, S.Y. and F.B.; formal analysis, S.Y. and F.B.; investigation, Y.L.; resources, Y.L.; data curation, S.Y., F.B. and X.Z.; writing—original draft preparation, S.Y.; writing—review and editing, Y.L. and F.B.; visualization, S.Y. and F.B.; supervision, Y.L.; project administration, Y.L.; funding acquisition, Y.L. All authors have read and agreed to the published version of the manuscript.

**Funding:** This research was funded by the Key Special Project for Introduced Talents Team of Southern Marine Science and Engineering at Guangdong Laboratory (Guangzhou) under grant number GML2019ZD0210; the National Natural Science Foundation of China under grant numbers

41961160728, 42105124, and 41575106; the Shenzhen Science and Technology Program under grant number KQTD20180411143441009; the Key-Area Research and Development Program of Guangdong Province under grant number 2020B1111360001; the Guangdong Basic and Applied Basic Research Fund under grant number 2019A1515110384; the Guangdong Province Science and Technology Planning Project of China under grant number 2017A050506003; and the NSFC/RGC (grant no. N\_HKUST638/19).

**Acknowledgments:** We are grateful to the editor and anonymous reviewers for their constructive comments. We want to acknowledge the provision of MODIS satellite data by the Ministry of Environmental Protection Data Center, US National Center for Atmospheric Research (NCAR), and the US National Aeronautics and Space Administration (NASA) Data Center, respectively; We thank the National Aeronautics and Space Administration (NASA) and PHOTONS for providing AERONET site data. We also would like to thank the National Oceanic and Atmospheric Administration (NOAA) Air Resources Laboratory (ARL) for providing the Hybrid Single-Particle Lagrangian Integrated Trajectory (HYSPLIT) model. We also thank Ricchiazzi et al. for providing the Santa Barbara DISORT Atmospheric Radiative Transfer (SBDART) software tool.

**Conflicts of Interest:** The authors declare no conflict of interest.

## References

- Houghton, R.A.; Skole, D.L.; Nobre, C.A.; Hackler, J.L.; Lawrence, K.T.; Chomentowski, W.H. Annual fluxes of carbon from deforestation and regrowth in the Brazilian Amazon. *Nature* **2000**, *403*, 301–304. [[CrossRef](#)] [[PubMed](#)]
- Tian, H.; Melillo, J.M.; Kicklighter, D.W.; McGuire, A.D.; Helfrich, J.V.K.; Moore, B.; Vörösmarty, C.J. Effect of interannual climate variability on carbon storage in Amazonian ecosystems. *Nature* **1998**, *396*, 664–667. [[CrossRef](#)]
- Cochrane, M.A.; Schulze, M.D. Fire as a Recurrent Event in Tropical Forests of the Eastern Amazon: Effects on Forest Structure, Biomass, and Species Composition. *Biotropica* **1999**, *31*, 2–16. [[CrossRef](#)]
- Laurance, W.F.; Albernaz, A.K.M.; Schroth, G.; Fearnside, P.M.; Bergen, S.; Venticinque, E.M.; Da Costa, C. Predictors of deforestation in the Brazilian Amazon. *J. Biogeogr.* **2002**, *29*, 737–748. [[CrossRef](#)]
- Siegert, F.; Ruecker, G.; Hinrichs, A.; Hoffmann, A.A. Increased damage from fires in logged forests during droughts caused by El Niño. *Nature* **2001**, *414*, 437–440. [[CrossRef](#)]
- Achard, F.; Eva, H.D.; Stibig, H.-J.; Mayaux, P.; Gallego, J.; Richards, T.; Malingreau, J.-P. Determination of Deforestation Rates of the World's Humid Tropical Forests. *Science* **2002**, *297*, 999–1002. [[CrossRef](#)]
- Skole, D.; Tucker, C. Tropical Deforestation and Habitat Fragmentation in the Amazon: Satellite Data from 1978 to 1988. *Science* **1993**, *260*, 1905–1910. [[CrossRef](#)]
- De Bem, P.P.; de Carvalho Junior, O.A.; Fontes Guimarães, R.; Trancoso Gomes, R.A. Change Detection of Deforestation in the Brazilian Amazon Using Landsat Data and Convolutional Neural Networks. *Remote Sens.* **2020**, *12*, 901. [[CrossRef](#)]
- De Area Leão Pereira, E.J.; de Santana Ribeiro, L.C.; da Silva Freitas, L.F.; de Barros Pereira, H.B. Brazilian policy and agribusiness damage the Amazon rainforest. *Land Use Policy* **2020**, *92*, 104491. [[CrossRef](#)]
- Bencherif, H.; Bègue, N.; Kirsch Pinheiro, D.; du Preez, D.J.; Cadet, J.-M.; da Silva Lopes, F.J.; Shikwambana, L.; Landulfo, E.; Vescovini, T.; Labuschagne, C.; et al. Investigating the Long-Range Transport of Aerosol Plumes Following the Amazon Fires (August 2019): A Multi-Instrumental Approach from Ground-Based and Satellite Observations. *Remote Sens.* **2020**, *12*, 3846. [[CrossRef](#)]
- Lizundia-Loiola, J.; Pettinari, M.L.; Chuvieco, E. Temporal Anomalies in Burned Area Trends: Satellite Estimations of the Amazonian 2019 Fire Crisis. *Remote Sens.* **2020**, *12*, 151. [[CrossRef](#)]
- Chung, C.E.; Ramanathan, V.; Decremer, D. Observationally constrained estimates of carbonaceous aerosol radiative forcing. *Proc. Natl. Acad. Sci. USA* **2012**, *109*, 11624–11629. [[CrossRef](#)] [[PubMed](#)]
- Malhi, Y.; Roberts, J.T.; Betts, R.A.; Killeen, T.J.; Li, W.; Nobre, C.A. Climate Change, Deforestation, and the Fate of the Amazon. *Science* **2008**, *319*, 169–172. [[CrossRef](#)]
- Ten Hoeve, J.E.; Remer, L.A.; Jacobson, M.Z. Microphysical and radiative effects of aerosols on warm clouds during the Amazon biomass burning season as observed by MODIS: Impacts of water vapor and land cover. *Atmos. Chem. Phys.* **2011**, *11*, 3021–3036. [[CrossRef](#)]
- Procopio, A.S.; Artaxo, P.; Kaufman, Y.J.; Remer, L.A.; Schafer, J.S.; Holben, B.N. Multiyear analysis of amazonian biomass burning smoke radiative forcing of climate. *Geophys. Res. Lett.* **2004**, *31*, L03108. [[CrossRef](#)]
- Zhang, Y.; Fu, R.; Yu, H.; Dickinson, R.E.; Juarez, R.N.; Chin, M.; Wang, H. A regional climate model study of how biomass burning aerosol impacts land-atmosphere interactions over the Amazon. *J. Geophys. Res. Atmos.* **2008**, *113*, D144S15. [[CrossRef](#)]
- Kolusu, S.R.; Marsham, J.H.; Mulcahy, J.; Johnson, B.; Dunning, C.; Bush, M.; Spracklen, D.V. Impacts of Amazonia biomass burning aerosols assessed from short-range weather forecasts. *Atmos. Chem. Phys.* **2015**, *15*, 12251–12266. [[CrossRef](#)]
- Da Silva Palácios, R.; Romera, K.S.; Curado, L.F.A.; Banga, N.M.; Rothmund, L.D.; da Silva Sallo, F.; Morais, D.; Santos, A.C.A.; Moraes, T.J.; Morais, F.G.; et al. Long Term Analysis of Optical and Radiative Properties of Aerosols in the Amazon Basin. *Aerosol Air Qual. Res.* **2020**, *20*, 139–154. [[CrossRef](#)]

19. Sena, E.T.; Artaxo, P. A novel methodology for large-scale daily assessment of the direct radiative forcing of smoke aerosols. *Atmos. Chem. Phys.* **2015**, *15*, 5471–5483. [[CrossRef](#)]
20. Feingold, G.; Jiang, H.; Harrington, J.Y. On smoke suppression of clouds in Amazonia. *Geophys. Res. Lett.* **2005**, *32*, L02804. [[CrossRef](#)]
21. Liu, L.; Cheng, Y.; Wang, S.; Wei, C.; Pöhlker, M.L.; Pöhlker, C.; Artaxo, P.; Shrivastava, M.; Andreae, M.O.; Pöschl, U.; et al. Impact of biomass burning aerosols on radiation, clouds, and precipitation over the Amazon: Relative importance of aerosol–cloud and aerosol–radiation interactions. *Atmos. Chem. Phys.* **2020**, *20*, 13283–13301. [[CrossRef](#)]
22. Ten Hoeve, J.E.; Jacobson, M.Z.; Remer, L.A. Comparing results from a physical model with satellite and in situ observations to determine whether biomass burning aerosols over the Amazon brighten or burn off clouds. *J. Geophys. Res. Atmos.* **2012**, *117*, D08203. [[CrossRef](#)]
23. Zhang, Y.; Fu, R.; Yu, H.; Qian, Y.; Dickinson, R.; Silva Dias, M.A.F.; da Silva Dias, P.L.; Fernandes, K. Impact of biomass burning aerosol on the monsoon circulation transition over Amazonia. *Geophys. Res. Lett.* **2009**, *36*, L10814. [[CrossRef](#)]
24. Hsu, N.C.; Tsay, S.-C.; King, M.D.; Herman, J.R. Aerosol properties over bright-reflecting source regions. *IEEE Geosci. Remote Sens. Lett.* **2004**, *42*, 557–569. [[CrossRef](#)]
25. Levy, R.C.; Mattoo, S.; Munchak, L.A.; Remer, L.A.; Sayer, A.M.; Patadia, F.; Hsu, N.C. The Collection 6 MODIS aerosol products over land and ocean. *Atmos. Meas. Tech.* **2013**, *6*, 2988–3034. [[CrossRef](#)]
26. Remer, L.A.; Kaufman, Y.J.; Tanré, D.; Mattoo, S.; Chu, D.A.; Martins, J.V.; Li, R.-R.; Ichoku, C.; Levy, R.C.; Kleidman, R.G.; et al. The MODIS Aerosol Algorithm, Products, and Validation. *J. Atmos. Sci.* **2005**, *62*, 947–973. [[CrossRef](#)]
27. Bao, F.; Li, Y.; Cheng, T.; Gao, J.; Yuan, S. Estimating the Columnar Concentrations of Black Carbon Aerosols in China Using MODIS Products. *Environ. Sci. Technol.* **2020**, *54*, 11025–11036. [[CrossRef](#)]
28. Chu, D.A.; Kaufman, Y.J.; Zibordi, G.; Chern, J.D.; Mao, J.; Li, C.; Holben, B.N. Global monitoring of air pollution over land from the Earth Observing System-Terra Moderate Resolution Imaging Spectroradiometer (MODIS). *J. Geophys. Res. Atmos.* **2003**, *108*, 4661. [[CrossRef](#)]
29. Koren, I.; Kaufman, Y.J.; Remer, L.A.; Martins, J.V. Measurement of the Effect of Amazon Smoke on Inhibition of Cloud Formation. *Science* **2004**, *303*, 1342–1345. [[CrossRef](#)]
30. Sayer, A.M.; Munchak, L.A.; Hsu, N.C.; Levy, R.C.; Bettenhausen, C.; Jeong, M.-J. MODIS Collection 6 aerosol products: Comparison between Aqua’s e-Deep Blue, Dark Target, and “merged” data sets, and usage recommendations. *J. Geophys. Res. Atmos.* **2014**, *119*, 965–989. [[CrossRef](#)]
31. Bohren, C.F.; Huffman, D.R. *Absorption and Scattering of Light by Small Particles*; John Wiley & Sons: Hoboken, NJ, USA, 2008; ISBN 978-3-527-61816-3.
32. Dubovik, O.; Holben, B.; Eck, T.F.; Smirnov, A.; Kaufman, Y.J.; King, M.D.; Tanré, D.; Slutsker, I. Variability of Absorption and Optical Properties of Key Aerosol Types Observed in Worldwide Locations. *J. Atmos. Sci.* **2002**, *59*, 590–608. [[CrossRef](#)]
33. Schuster, G.L.; Dubovik, O.; Holben, B.N. Angstrom exponent and bimodal aerosol size distributions. *J. Geophys. Res. Atmos.* **2006**, *111*, D7. [[CrossRef](#)]
34. Wiscombe, W.J. Improved Mie scattering algorithms. *Appl. Opt.* **1980**, *19*, 1505–1509. [[CrossRef](#)] [[PubMed](#)]
35. Holben, B.N.; Eck, T.F.; Slutsker, I.; Tanré, D.; Buis, J.P.; Setzer, A.; Vermote, E.; Reagan, J.A.; Kaufman, Y.J.; Nakajima, T.; et al. AERONET—A Federated Instrument Network and Data Archive for Aerosol Characterization. *Remote Sens. Environ.* **1998**, *66*, 1–16. [[CrossRef](#)]
36. Chang, H.; Charalampopoulos, T.T. Determination of the wavelength dependence of refractive indices of flame soot. *Proc. R. Soc. London. Ser. A Math. Phys. Sci.* **1990**, *430*, 577–591. [[CrossRef](#)]
37. Ganguly, D.; Ginoux, P.; Ramaswamy, V.; Dubovik, O.; Welton, J.; Reid, E.A.; Holben, B.N. Inferring the composition and concentration of aerosols by combining AERONET and MPLNET data: Comparison with other measurements and utilization to evaluate GCM output. *J. Geophys. Res. Atmos.* **2009**, *114*, D16203. [[CrossRef](#)]
38. Giles, D.M.; Sinyuk, A.; Sorokin, M.G.; Schafer, J.S.; Smirnov, A.; Slutsker, I.; Eck, T.F.; Holben, B.N.; Lewis, J.R.; Campbell, J.R.; et al. Advancements in the Aerosol Robotic Network (AERONET) Version 3 database—automated near-real-time quality control algorithm with improved cloud screening for Sun photometer aerosol optical depth (AOD) measurements. *Atmos. Meas. Tech.* **2019**, *12*, 169–209. [[CrossRef](#)]
39. Holben, B.N.; Eck, T.F.; Slutsker, I.; Smirnov, A.; Sinyuk, A.; Schafer, J.; Giles, D.; Dubovik, O. Aeronet’s Version 2.0 Quality Assurance Criteria. In *Remote Sensing of the Atmosphere and Clouds*; SPIE: Goa, India, 2006; Volume 6408, pp. 134–147.
40. Wang, L.; Li, Z.; Tian, Q.; Ma, Y.; Zhang, F.; Zhang, Y.; Li, D.; Li, K.; Li, L. Estimate of aerosol absorbing components of black carbon, brown carbon, and dust from ground-based remote sensing data of sun-sky radiometers. *J. Geophys. Res. Atmos.* **2013**, *118*, 6534–6543. [[CrossRef](#)]
41. Ricchiuzzi, P.; Yang, S.; Gautier, C.; Sowle, D. SBDART: A Research and Teaching Software Tool for Plane-Parallel Radiative Transfer in the Earth’s Atmosphere. *Bull. Am. Meteorol. Soc.* **1998**, *79*, 2101–2114. [[CrossRef](#)]
42. Ramana, M.V.; Ramanathan, V.; Feng, Y.; Yoon, S.-C.; Kim, S.-W.; Carmichael, G.R.; Schauer, J.J. Warming influenced by the ratio of black carbon to sulphate and the black-carbon source. *Nat. Geosci.* **2010**, *3*, 542–545. [[CrossRef](#)]
43. Saleh, R.; Robinson, E.S.; Tkacik, D.S.; Ahern, A.T.; Liu, S.; Aiken, A.C.; Sullivan, R.C.; Presto, A.A.; Dubey, M.K.; Yokelson, R.J.; et al. Brownness of organics in aerosols from biomass burning linked to their black carbon content. *Nat. Geosci.* **2014**, *7*, 647–650. [[CrossRef](#)]

44. Bond, T.C.; Bergstrom, R.W. Light Absorption by Carbonaceous Particles: An Investigative Review. *Aerosol Sci. Technol.* **2007**, *40*, 1. [[CrossRef](#)]
45. Bond, T.C.; Doherty, S.J.; Fahey, D.W.; Forster, P.M.; Bernsten, T.; DeAngelo, B.J.; Flanner, M.G.; Ghan, S.; Kärcher, B.; Koch, D.; et al. Bounding the role of black carbon in the climate system: A scientific assessment. *J. Geophys. Res. Atmos.* **2013**, *118*, 5380–5552. [[CrossRef](#)]
46. Giglio, L.; Desloîtres, J.; Justice, C.O.; Kaufman, Y.J. An Enhanced Contextual Fire Detection Algorithm for MODIS. *Remote Sens. Environ.* **2003**, *87*, 273–282. [[CrossRef](#)]
47. Stein, A.F.; Draxler, R.R.; Rolph, G.D.; Stunder, B.J.B.; Cohen, M.D.; Ngan, F. NOAA’s HYSPLIT Atmospheric Transport and Dispersion Modeling System. *Bull. Am. Meteorol. Soc.* **2015**, *96*, 2059–2077. [[CrossRef](#)]
48. Chakraborty, M.; Dey, G.; Gupta, R.K.P. *Satellite Based Study on Amazon Rain Forest Fires and Effect on Climate*; Social Science Research Network: Rochester, NY, USA, 2019.
49. Bandopadhyay, S.; Sánchez, D.A.C. Amazonian Fire Events Disturbed the Global Carbon Cycle: A Study from 2019 Amazon Wildfire Using Google Earth Engine. *Environ. Sci. Proc.* **2020**, *3*, 43. [[CrossRef](#)]
50. Sena, E.T.; Artaxo, P.; Correia, A.L. Spatial variability of the direct radiative forcing of biomass burning aerosols and the effects of land use change in Amazonia. *Atmos. Chem. Phys.* **2013**, *13*, 1261–1275. [[CrossRef](#)]
51. Ramanathan, V.; Carmichael, G. Global and regional climate changes due to black carbon. *Nat. Geosci.* **2008**, *1*, 221–227. [[CrossRef](#)]
52. Bao, F.; Cheng, T.; Li, Y.; Shi, S.; Guo, H.; Wu, Y. Single Scattering Albedo of High Loading Aerosol Estimated Across East Asia From S-NPP VIIRS. *IEEE Trans. Geosci. Remote Sens.* **2022**, *60*, 1–11. [[CrossRef](#)]
53. Ramanathan, V.; Crutzen, P.J.; Lelieveld, J.; Mitra, A.P.; Althausen, D.; Anderson, J.; Andreae, M.O.; Cantrell, W.; Cass, G.R.; Chung, C.E.; et al. Indian Ocean Experiment: An integrated analysis of the climate forcing and effects of the great Indo-Asian haze. *J. Geophys. Res. Atmos.* **2001**, *106*, 28371–28398. [[CrossRef](#)]
54. Bond, T.C.; Sun, H. Can Reducing Black Carbon Emissions Counteract Global Warming? *Environ. Sci. Technol.* **2005**, *39*, 5921–5926. [[CrossRef](#)] [[PubMed](#)]
55. Nobre, C.A.; Sampaio, G.; Borma, L.S.; Castilla-Rubio, J.C.; Silva, J.S.; Cardoso, M. Land-use and climate change risks in the Amazon and the need of a novel sustainable development paradigm. *Proc. Natl. Acad. Sci. USA* **2016**, *113*, 10759–10768. [[CrossRef](#)] [[PubMed](#)]
56. Dos Santos, F.S.; Pinto, J.A.; Maciel, F.M.; Horta, F.S.; de Almeida Albuquerque, T.T.; de Fátima Andrade, M. Avaliação da influência das condições meteorológicas na concentração de material particulado fino (MP<sub>2,5</sub>) em Belo Horizonte, MG. *Eng. Sanit. Ambient.* **2019**, *24*, 371–381. [[CrossRef](#)]
57. Mano, A.; Samora, R. Brazil on Drought Alert, Faces Worst Dry Spell in 91 Years. Reuters. 2021. Available online: <https://www.reuters.com/business/environment/brazil-drought-alert-country-faces-worst-dry-spell-91-years-2021-05-28/> (accessed on 29 May 2021).
58. Amazon Fire Activity in 2020 Surpasses 2019—Global Fire Emissions Database. Available online: <https://globalfiredata.org/pages/2020/09/22/amazon-fire-activity-in-2020-surpasses-2019/> (accessed on 22 September 2020).